# Spatio-temporal structure of storm-time chorus

O Santolík, D S Gurnett, J S Pickett, Michel Parrot

# Spatio-temporal structure of storm-time chorus

O. Santolík,[1] D. A. Gurnett, and J. S. Pickett
Department of Physics and Astronomy, University of Iowa, Iowa City, USA

M. Parrot
LPCE/CNRS, Orléans, France

N. Cornilleau-Wehrlin
CETP, Vélizy, France

Received 22 November 2002; revised 17 March 2003; accepted 17 April 2003; published 9 July 2003.

[1] We discuss chorus emissions measured by the four Cluster spacecraft at close separations during a geomagnetically disturbed period on 18 April 2002. We analyze the lower band of chorus below one half of the electron cyclotron frequency, measured at a radial distance of 4.4 Earth's radii, within a 2000 km long source region located close to the equator. The characteristic wave vector directions in this region are nearly parallel to the field lines and the multipoint measurement demonstrates the dynamic character of the chorus source region, changing the Poynting flux direction at time scales shorter than a few seconds. The electric field waveforms of the chorus wave packets (forming separate chorus elements on power spectrograms) show a fine structure consisting of subpackets with a maximum amplitude above 30 mV/m. To study this fine structure we have used a sine-wave parametric model with a variable amplitude. The subpackets typically start with an exponential growth phase, and after reaching the saturation amplitude they often show an exponential decay phase. The duration of subpackets is variable from a few milliseconds to a few tens of milliseconds, and they appear in the waveform randomly, with no clear periodicity. The obtained growth rate (ratio of the imaginary part to the real part of the wave frequency) is highly variable from case to case with values obtained between a few thousandths and a few hundredths. The same chorus wave packets simultaneously observed on the different closely separated spacecraft appear to have a different internal subpacket structure. The characteristic scale of the subpackets can thus be lower than tens of kilometers in the plane perpendicular to the field line, or hundreds of kilometers parallel to the field line (corresponding to a characteristic time scale of few milliseconds during the propagation of the entire wave packet). Using delays of time-frequency curves obtained on different spacecraft, we have found the same propagation direction as obtained from the simultaneous Poynting flux calculations. The delays roughly correspond to the whistler-mode group velocity estimated from the cold plasma theory. We have also observed delays corresponding to antiparallel propagation directions for two neighboring chorus wave packets, less than 0.1 s apart. *INDEX TERMS:* 2772 Magnetospheric Physics: Plasma waves and instabilities; 2730 Magnetospheric Physics: Magnetosphere—inner; 6939 Radio Science: Magnetospheric physics; 2778 Magnetospheric Physics: Ring current; 6984 Radio Science: Waves in plasma; *KEYWORDS:* storm-time chorus emissions, whistler mode, propagation analysis, parametric waveform analysis, multipoint measurements, Cluster

**Citation:** Santolík, O., D. A. Gurnett, J. S. Pickett, M. Parrot, and N. Cornilleau-Wehrlin, Spatio-temporal structure of storm-time chorus, *J. Geophys. Res.*, *108*(A7), 1278, doi:10.1029/2002JA009791, 2003.

## 1. Introduction

[2] Chorus emissions are plasma waves propagating through the Earth's magnetosphere in the whistler mode at frequencies between a few hundreds of hertz to several kHz. They consist of discrete elements, which we will refer to as wave packets, each of which lasts for a time on the order of

[1] Permanently at Faculty of Mathematics and Physics, Charles University, Prague, and at Institute of Atmospheric Physics, Czech Academy of Sciences, Prague, Czech Republic.


0148-0227/03/2002JA009791

a tenth to a few tenths of a second. In each chorus wave packet the frequency changes with a typical rate of a few kHz/s; more often it increases, but falling tones are also observed. These very intense natural emissions have been studied for several decades [*Gurnett and O'Brien*, 1964; *Helliwell*, 1965; *Dunkel and Helliwell*, 1969] and received a lot of attention in the past (see, e.g., reviews by *Omura et al.* [1991] or *Sazhin and Hayakawa* [1992]) but their generation mechanism is still not well understood.

[3] Recent experimental work was directed toward the localization of the source region [e.g., *LeDocq et al.*, 1998; *Parrot et al.*, 2003], propagation and time-frequency characteristics of chorus [e.g., *Nagano et al.*, 1996; *Gurnett et al.*, 2001] and properties of the chorus source [e.g., *Skoug et al.*, 1996; *Lauben et al.*, 1998]. Despite some controversies and contradictory results, it is often accepted that generation of chorus is a nonlinear process [e.g., *Nunn et al.*, 1997; *Trakhtengerts*, 1999] connected with the electron cyclotron resonance of radiation belt electrons and whistler-mode waves [*Helliwell*, 1967] that propagate parallel to the ambient magnetic field [e.g., *Hayakawa et al.*, 1984; *Goldstein and Tsurutani*, 1984] and that it takes place close to the geomagnetic equatorial plane [e.g., *Burtis and Helliwell*, 1969; *Burton and Holzer*, 1974; *LeDocq et al.*, 1998]. Nightside chorus observed during geomagnetic storms is especially interesting for the investigation of the source mechanism [e.g., *Anderson and Maeda*, 1977; *Meredith et al.*, 2000].

[4] The linear theory of the cyclotron instability [*Kennel and Petschek*, 1966] has been recently reexamined by *Pasmanik et al.* [2002] who found large convective amplification factors for step-like electron distribution functions. For large amplitude waves, studies using a one-dimensional (1-D) Vlasov Hybrid Simulation code [see *Nunn et al.*, 1997 and references therein] found that nonlinear growth rates can be larger than the linear ones by a factor of 2–5. In the nonlinear theory an absolute instability responsible for a rapid wave growth everywhere in the source region is considered [*Nunn et al.*, 1997; *Smith and Nunn*, 1998; *Trakhtengerts*, 1999; A. G. Demekhov et al., Backward wave oscillator regime of whistler cyclotron instability in an inhomogeneous magnetic field, submitted to *Physics of Plasmas*, 2003].

[5] In this paper we analyze propagation and time-frequency characteristics of nightside chorus during a geomagnetically disturbed period. We use simultaneous observations of intense waves by four Cluster spacecraft localized in the source region close to the geomagnetic equator at a radial distance of 4.4 $R_E$. Our analysis is mainly based on high-resolution measurements of the wideband (WBD) wave instruments [*Gurnett et al.*, 2001], and the multidimensional data of the spectrum analyzers of the STAFF instruments [*Cornilleau-Wehrlin et al.*, 2003]. We also use supporting data of the Whisper sounders [*Décréau et al.*, 2001], and measurements of the onboard flux-gate magnetometers (FGM) [*Balogh et al.*, 2001].

[6] In section 2 we will present the observations and show results of analysis at spatial scales of the order of $10^3$ km and temporal scales from several seconds to one hour. Section 3 will describe the results of analysis of individual chorus wave packets at spatial scales of tens to hundreds of kilometers and time intervals of units to tens of milliseconds, and finally, in section 4 we will summarize the results.

## 2. Observations of the Chorus Source Region

[7] Figure 1 shows an overview plot of measurements of intense chorus on 18 April 2002. The Cluster spacecraft passed through their perigee at a radial distance of 4.4 $R_E$, at 2100 MLT, and close to the magnetic equatorial plane, while the hourly equatorial Dst index decreased to −126 nT at 0800 UT and to −116 nT at 0900 UT. These disturbances were accompanied by substorm activity, reflected by the AE index fluctuating between 500 and 1100 nT around 0900 UT. The geomagnetically disturbed conditions are also shown by Kp indices which were $7^\circ$, $7^-$, and $6^-$ in the first three 3-hour intervals on 18 April 2002. Significant irregular variations of the magnetic field were also observed along the Cluster orbit: the white lines in Figure 1a show the local electron cyclotron frequency ($f_{ce}$), and one half of $f_{ce}$, both being proportional to the field strength obtained from the FGM data. Under normal conditions near the Cluster perigee this parameter varies smoothly, following predominantly the changes of the radial distance and magnetic latitude along the orbit. On 18 April 2002, however, $f_{ce}$ was about 20% lower than under undisturbed conditions and its variations were irregular. These disturbances were accompanied by generation of intense chorus emissions. While the spacecraft moved along its orbit through the equatorial region from the South to the North, the WBD instruments on all the four spacecraft made continuous measurements using a pass-band filter between 70 Hz and 10 kHz, a sampling frequency of 27.44 kHz, and the 8-bit quantization mode. An 88-m electric double-sphere antenna [*Gustafsson et al.*, 2001] was used as a sensor most of the time, except small intervals of about 10 s, repeating every ≈50 s. During these intervals the input was switched to a magnetic search-coil antenna; we do not use those data in the present study, and the resulting data gaps are interpolated in Figure 1a.

[8] The chorus emissions in Figure 1a are organized into two bands separated by a gap of decreased power, similar to previous observations of, e.g., *Anderson and Maeda* [1977]. The lower-frequency limit of the upper band follows the local $\frac{1}{2} f_{ce}$. At higher latitudes above $+5^\circ$ in the Northern Hemisphere and below $-5^\circ$ in the Southern Hemisphere the upper band of chorus disappears, and the lower band decreases in frequency down to less than one tenth of the local $f_{ce}$. The lower-band chorus propagates as electromagnetic waves as it is demonstrated in Figure 1b by simultaneous measurements of intense magnetic fluctuations by the STAFF-SA instrument [*Cornilleau-Wehrlin et al.*, 1997]. The upper frequency limit of this instrument at 4 kHz is close to $\frac{1}{2} f_{ce}$ in the equatorial region and thus its measurement is limited to the lower band of chorus. Although the data have a lower time resolution (4 s) and frequency resolution (25%) compared with the waveform WBD data, the STAFF-SA instrument provides us with results of multidimensional spectral analysis performed onboard with three magnetic and two electric components. We use these data to calculate the parameters shown in Figures 1c–1d.

[9] From cross-spectra of electric and magnetic field fluctuations we estimate the parameter $S_\parallel/\sigma S_\parallel$, where $S_\parallel$ is

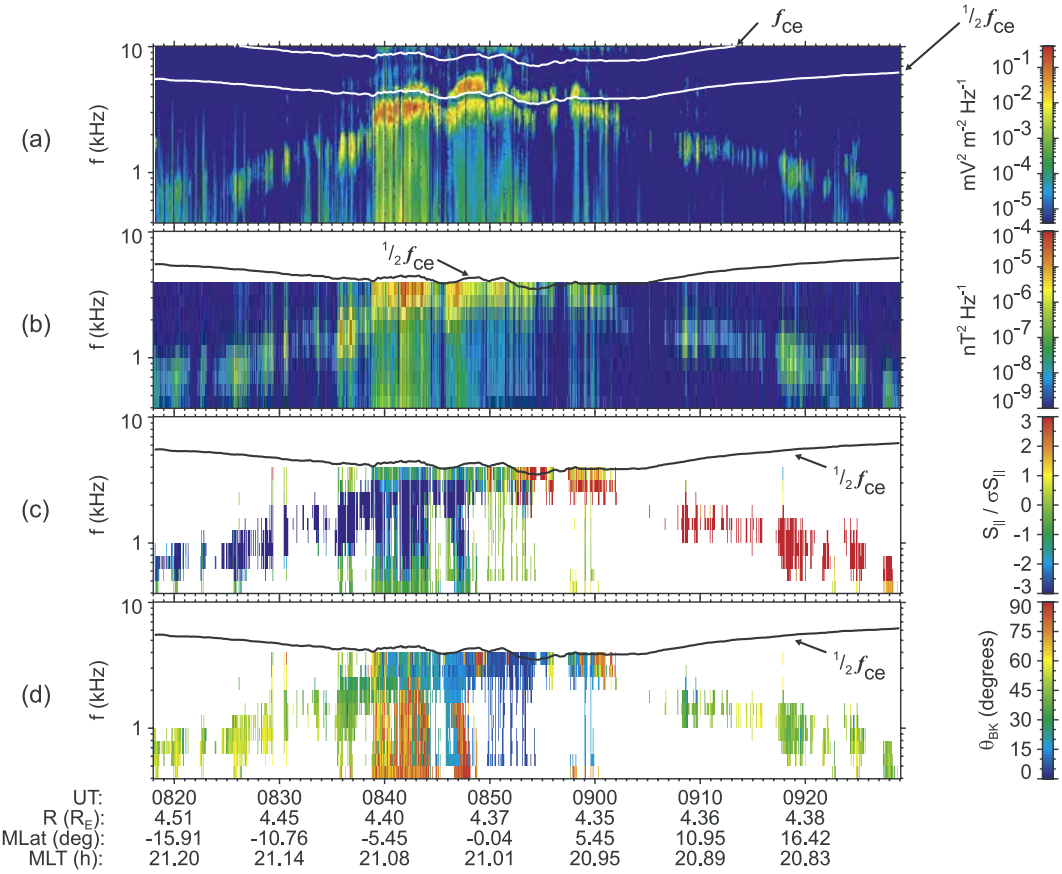


**Figure 1.** Overview plot of large-scale structure of chorus observed by Cluster 4 on 18 April 2002. (a) Time-frequency power spectrogram of electric field fluctuations recorded by the WBD instrument. Overplotted white lines indicate $\frac{1}{2} f_{ce}$ and $f_{ce}$. (b) Power spectrogram of magnetic field fluctuations measured by the STAFF-SA instrument. (c) Parallel component of the Poynting vector normalized by its standard deviation. (d) Angle deviation between $\boldsymbol{k}$ and $\boldsymbol{B}_0$ vectors. The results in Figures 1c–1d are plotted only if the magnetic power spectral density (Figure 1b) is higher than $10^{-8}$ $nT^2Hz^{-1}$. Position is given on the bottom: R-radial distance; MLat-magnetic dipole latitude; MLT-magnetic local time.

proportional to the projection of the Poynting vector to the direction of the ambient magnetic field ($\boldsymbol{B}_0$), and the normalization factor $\sigma\ S_{||}$ corresponds to an estimate of the standard deviation of $S_{||}$ from errors induced by the spectral analysis (see equation (8) of *Santolík et al.* [2001]). Since $\sigma\ S_{||}$ is always positive, the sign of the parameter $S_{||}/\sigma S_{||}$ shows if the Poynting flux has a component parallel to $\boldsymbol{B}_0$ (northward in the equatorial region) or antiparallel to $\boldsymbol{B}_0$ (southward). Results in Figure 1c show that the Poynting flux mainly has a southward component (blue) at negative magnetic latitudes and northward component (red) at positive magnetic latitudes. This means that the projection of the Poynting flux to the $\boldsymbol{B}_0$ direction points away from the magnetic equatorial region. Since the analyzed chorus waves are in the whistler mode (as indicated also by the right-hand polarization observed by STAFF-SA) at frequencies between the lower hybrid frequency and $\frac{1}{2} f_{ce}$, the Poynting vector has to be at small angles with respect to $\boldsymbol{B}_0$, and the observed divergence of the Poynting flux indicates that the source region is localized within a few degrees of magnetic latitude from the equatorial plane. Similar results were previously obtained, e.g., by *LeDocq et al.* [1998]. In the source region close to the magnetic equatorial plane the predominant direction fluctuates, and often it cannot be reliably determined with the 4-s time resolution of STAFF-SA measurements. These observations will be discussed later on in more detail, using the data of the four Cluster spacecraft.

[10] Analysis of magnetic field fluctuations by the method of *Santolík et al.* [2003] gives us an average angle deviation $\theta_{BK}$ of the wave vector $\boldsymbol{k}$ from $\boldsymbol{B}_0$, corresponding to a characteristic plane wave. Since we only use the wave magnetic field, the results are identical for any two antiparallel wave vectors. We thus give the results in the interval $\langle 0°, 90° \rangle$, and, for example, $\theta_{BK} = 0°$ for both parallel and antiparallel directions with respect to $\boldsymbol{B}_0$. Figure 1d demonstrates that this angle is most often below 10° in the chorus source region. We have obtained very similar results when we processed the STAFF-SA by other techniques, for example by the method of *Samson* [1973]. These results are in a rough agreement with the previous observations of, e.g., *Hayakawa et al.* [1984], and they are also principally consistent with the widely accepted cyclotron resonance generation mechanism [e.g., *Trakhtengerts*, 1999]. Propagating from the source to higher latitudes on both sides of the equator, the characteristic wave vectors of chorus gradually

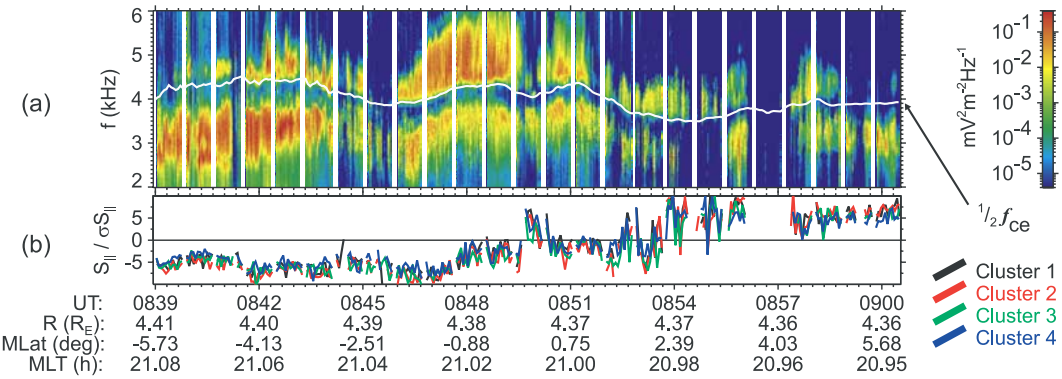


**Figure 2.** (a) Time-frequency power spectrogram of electric field fluctuations recorded by the WBD instrument by Cluster 1 close to the source of chorus on 18 April 2002. Over-plotted white line indicates $\frac{1}{2} f_{ce}$. (b) Parallel component of the Poynting vector normalized by its standard deviation from the measurement of the STAFF-SA instruments on board the four Cluster spacecraft (spacecraft indicated by different colors). Position is given on the bottom for Cluster 1 in the same format as in Figure 1.

incline from the $\boldsymbol{B}_0$ direction up to angles of ≈60° at magnetic latitudes below −10° and above +10° However, we can note sporadic occurrences of very high values of $\theta_{BK}$ also in the source region. Analysis of these anomalies is, however, out of the scope of the present paper. Although Figure 1 is plotted using the data of the single Cluster 4 spacecraft, there is no need to show such plots for the other three spacecraft because they provide us with very similar results. The reason for that similarity is that the four spacecraft were in this period of time located very close to each other, the maximum separation being less than 300 km.

[11] A closer look at the source region is shown in Figure 2a using a spectrogram with a linear frequency scale. The white vertical lines repeating on the spectrogram every ≈50 s replace the data gaps where the electric field was not measured. We only plot a band between 2 and 6 kHz and only a portion of the orbit within ≈5° from the magnetic equator, where the analysis shown in Figure 1c indicated both southward and northward propagation. We can clearly see that the lower limit of the upper band of chorus corresponds to highly fluctuating values of $\frac{1}{2} f_{ce}$. Figure 2b shows a better localization of the chorus source region. We integrate the STAFF-SA data in the frequency range 1.6–4.0 kHz to increase the statistical significance of results, and, using the same method as in Figure 1c, we calculate $S_{||}/\sigma S_{||}$. We can clearly see that the parallel component of the Poynting flux is directed southward (negative values) at magnetic latitudes below −1° and northward (positive values) at magnetic latitudes above +3° In the interval between −1° and +3° the predominant direction fluctuates or cannot be reliably determined with the 4-s time resolution of the STAFF-SA data. This 4° interval of magnetic latitudes close to the equatorial plane is our best localization of the region where generation of lower-band chorus takes place. Note that this interval coincides with the interval where quasi-parallel average wave-vector directions prevail in Figure 1d.

[12] The 4° interval of magnetic latitudes corresponds to a length of ≈2000 km measured along the field line. Since our results also confirm that the waves, on average, propagate along the field lines, this length sets up an lower limit for the parallel extent of the source region of chorus. We can then compare this length with the theoretical estimations of the length of the resonance region. The Whisper data give us an estimate of characteristic plasma frequency (P. Canu, private communication, 2002) [*Canu et al.*, 2001] of approximately 12 kHz in the source region. Assuming a wave frequency of 3 kHz and an electron cyclotron frequency of 8 kHz, we obtain from equation (22) of *Helliwell* [1967] the length of the resonance region $l$ = 3230 km, i.e., the distance on which the wave and the resonating particle remain in phase, or the phase between the wave and the resonating particles has not varied by more than 180°. This, as the length over which the chorus amplitude increases to its final value, is compatible with the rough estimate of the interaction length according to *Trakhtengerts* [1999], 1550 km < $l$ < 12500 km. We take here his equation (11) which accounts for nonlinear effects on the frequency change as the lower limit of $l$, and his equation (17) which uses the cyclotron resonance condition for different frequencies to obtain the upper limit of $l$. In this estimate we assume that the wave frequency varies between 2.5 and 3.5 kHz. We also estimate the whistler-mode wavelength as approximately 30 km, using the measured plasma parameters and the cold plasma theory [*Stix*, 1992]. In any of these theories the parallel extent of the typical source is higher or comparable to the obtained 2000-km length of the region where the central positions of the sources are localized.

[13] The relative position of the four Cluster spacecraft in the source region close to the geomagnetic equator is shown in Figure 3. We use the local field aligned coordinates (LBA) whose $Z_{LBA}$ axis is parallel to $\boldsymbol{B}_0$ and the $X_{LBA}$ axis is in the plane of the local magnetic meridian, pointing outwards from the Earth. The origin is defined by the center of mass of the four spacecraft, which was at a magnetic latitude of −0.37° at 0849:30. The separation was largest between Cluster 1 and Cluster 3, reaching 270 km, oriented mainly along the field line. In the perpendicular plane, their separation was 74 km, while it was only 6 km between Cluster 1 and Cluster 2 which were close to the same field line. During their orbital motion the spacecraft moved approximately in the $+Z_{LBA}$ direction, at a speed of ≈4.5 km/s. This means that Cluster 3 was delayed by 1min on the orbit after the leading Cluster 1.

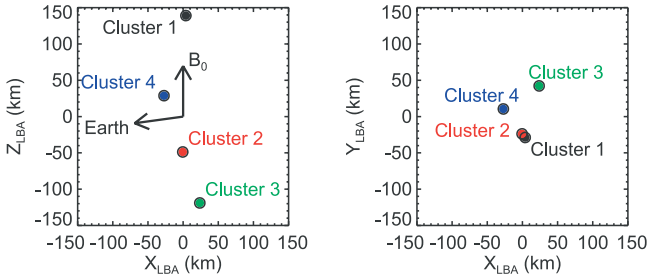


**Figure 3.** Relative position of the four Cluster spacecraft at 0849:30UT. Local field aligned coordinates are used in two projections: (left) to the plane of the local magnetic meridian; (right) to the plane perpendicular to the local magnetic field $\boldsymbol{B}_0$.

[14] Examining Figure 2b we can see that no such delay appears in the Poynting flux data. The observed variations of the Poynting flux were thus temporal and not spatial once the spacecraft reached the generation region. That means that within its ≈2000 km extent along the magnetic field lines, the actual source of chorus is not a stable feature localized in space but that it changes its directional properties at time scales shorter or comparable to the 4-s time resolution of the STAFF-SA instrument. These observations could be alternatively consistent with smaller sources reappearing at different places in the broader generation region and they also do not rule out the possibility that the chorus sources are very rapidly moving, as U.S. Inan (private communication, 2002) has recently suggested and as *Helliwell* [1967] previously discussed for discrete emissions in general.

## 3. Multipoint Analysis of Separate Chorus Wave Packets

[15] Figure 4 shows detailed power spectrograms from the WBD instruments on board all four Cluster spacecraft in the source region during a portion of the time period plotted in Figure 2. The time scale is chosen to allow detection of separate chorus wave packets below $\frac{1}{2}f_{ce}$. The four satellites were localized slightly to the south of the magnetic equator during this 6-s time interval. The band above the local $\frac{1}{2}f_{ce}$ contains intense hiss-like emissions with no clear demonstration of separate chorus wave packets. However, these waves rapidly change their intensity and the spectrograms are much more structured compared for instance with the spectrograms of plasmaspheric hiss observed during other orbits of Cluster spacecraft. Moreover, the band above the local $\frac{1}{2}f_{ce}$ does contain well-defined discrete chorus elements in other portions of the time period covered by Figure 2, as we will show later on. We thus use the common term "chorus" for all these emissions shown in Figures 1 and 2, knowing that the classical chorus elements are not always present and speculating that all these waves have a common origin.

[16] The band below $\frac{1}{2}f_{ce}$ generally is more structured, but in Figure 4 we can only see two well-defined chorus elements during the 6-s time interval. As we will show later on, this situation facilitates our analysis. Besides these two intense chorus wave packets recorded after 0849:30

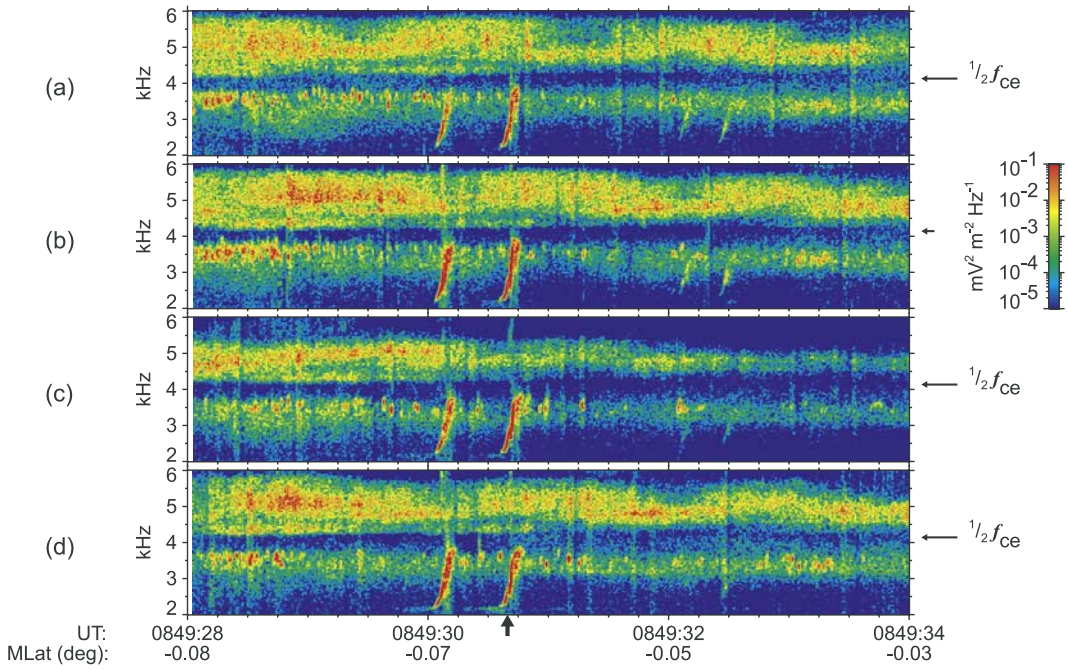


**Figure 4.** Detailed time-frequency power spectrograms of electric field fluctuations in the source region recorded by the WBD instruments on board all the four Cluster spacecraft on 18 April 2002 after 0849:28 UT. Figures 4a–4c show data from Cluster 1–4, respectively. Horizontal arrows on the right indicate local $\frac{1}{2}f_{ce}$ for each spacecraft. Magnetic latitude (MLat) is given on the bottom for Cluster 1. Cluster 2–4 are shifted by −0.39°, −0.53°, and −0.25° respectively. A bold vertical arrow on the bottom points to the chorus element which is chosen for further analysis (see text).

**Table 1.** Propagation Analysis for Chorus in Figure 4

| S/C | Time interval | Frequency interval | $S_{\|\|}/\sigma\ S_{\|\|}$ | $\theta_{BK}$ |
|---|---|---|---|---|
| 1 | 0849:30.60–0849:34.44 | 2000–2520 Hz | −4.8 | 12° |
| 2 | 0849:30.43–0849:34.27 | 2000–2520 Hz | −6.3 | 9° |
| 3 | 0849:30.21–0849:34.05 | 2000–2520 Hz | −6.1 | 7° |
| 4 | 0849:29.79–0849:33.63 | 2000–2520 Hz | −3.8 | 6° |

between 2.2 and 4 kHz, the spectrogram shows a weak background of hiss-like emissions accompanied by impulsive narrow band elements at a frequency around 3.5 kHz. These impulses most often occur before 0849:30, and there is no clear correlation between the separate impulses observed by the different spacecraft. On the other hand we can see that the two intense chorus wave packets are detected simultaneously by the four spacecraft. On Cluster 4 we can note that the two elements are preceded by weak emissions at frequencies around 2.2 kHz, i.e., at the lower edge of frequency interval occupied by the elements. This is similar to observations of *Hattori et al.* [1991], and it could also be possible that the two distinct risers are discrete emissions triggered off the weak noise band around 2.2 kHz. Both discrete wave packets are rising in frequency at an approximate rate of 15 kHz/s and these time-frequency characteristics appear to be very similar on the four different spacecraft. We have chosen the second element, denoted by a bold vertical arrow below the bottom spectrogram, for further analysis.

[17] Table 1 summarizes the propagation parameters obtained from the STAFF-SA data in a 3.84-s time interval and a 520-Hz frequency interval containing that chorus element. We use the same analysis methods as described in section2. We can see that the waves in this interval propagate approximately along the field lines, with $\theta_{BK} \approx 10°$, and that the Poynting flux has a component antiparallel to the $\boldsymbol{B}_0$ direction (to the south). The chorus element is the only intense emission in the time-frequency interval under consideration, except on Cluster 4 where both elements from Figure 4 are averaged. The wave packet should thus arrive at a different time at each of the different spacecraft, according to their parallel separation distances. For a typical parallel propagating wave at 3.5 kHz, the cold plasma theory [*Stix*, 1992] gives us an estimate of the group speed of $0.35c$ ($c$ is the speed of the light), using the measured plasma density and field strength. That means that Cluster 1, which is most on the north of the four spacecraft, should observe the packet ≈2.5 ms earlier than the most southward Cluster 3 spacecraft (see Figure 3).

[18] The timing accuracy of the WBD measurements should have been sufficient to detect this delay. Unfortunately, on this particular day, determination of the timing accuracy is not exact for the following reason: The incoming data recorders of the Deep Space Network (DSN) apply a ground-based time tag to each WBD transfer frame that allows us to obtain a reconstructed absolute time of measurement on each of the spacecraft with an accuracy of 10–12 μs. This accuracy has been verified for Cluster 2, whose data on 18 April 2002 were received by the Canberra DSN station and were independently time tagged by two separate recorders. The time tags agree to less than 1 μs, where the acceptable jitter allowed by DSN when applying these time tags is 2 μs. Obtaining two files with independent time tags provides one method of crosschecking for possible time tag errors, which do occur from time to time and which are not apparent unless a crosscheck of some kind is applied. For the data from the other three spacecraft, received by the Goldstone DSN station, no such verification was possible since only one recorder was used to apply the time tags. Based on our analysis of the ground receive time tags contained in hundreds of WBD data files and of the comparison of these time tags to those obtained from the onboard time counter (accuracy of 1–2 ms) contained in the WBD transfer frame, we believe that the accuracy of the ground receive time tags for all spacecraft on 18 April 2002 is at least as good as 100 μs. The accuracy of the relative timing is thus expected to be better than approximately 200 μ*s*, which is less than 10% of the expected time delay.

[19] This short delay of signals with a rising frequency, however, collides with the uncertainty principle of the spectral analysis: A time resolution $\Delta t$ better than 2.5 ms implies a frequency resolution $\Delta f \approx 1/\Delta t > 400$ Hz. With the observed frequency drift $f/t \approx 15$ kHz/s, this frequency resolution is insufficient since we cannot suppose that the amplitude of the signal does not vary [e.g., *Storey*, 1953]. We would need a frequency resolution $\Delta f \approx \Delta t \times \Delta f/t < 40$ Hz to prevent mixing of time delays in different frequency intervals. This maximum $\Delta f$ value is by an order of magnitude lower than what is possible while using methods of spectral analysis based on the Fourier transform or on the wavelet transform.

[20] We have therefore chosen to use a parametric method based on a nonlinear least-squares optimization of parameters of a sine wave model with a polynomially variable amplitude (see Appendix A for details). Prior to the analysis we use a digital pass-band filter to obtain the waveform data in a predefined frequency interval. We then divide the total time interval of the signal into small subintervals and we fit the model to these consecutive subintervals of data. Each of them has ≈1 ms duration (i.e., a few wave periods) and we obtain estimates of wave frequency $f$, phase $\varphi$, and amplitude $A$ on each such subinterval. We reject all these results when the filtered waveform is by more that 50% different from the original wide-band waveform on a given subinterval, i.e., when the signal is stronger outside the predefined frequency interval than inside it. We also reject all the results when the model does not fit the data within the 5% accuracy limit (see Appendix A). Additionally, the obtained frequency values are rejected when a conservative estimate of their absolute error is larger than 10 Hz. With the frequency drift of ≈15 kHz/s, this limit ensures a timing accuracy of 0.7 ms between the same chorus wave packets measured by the different spacecraft.

[21] The results are shown in Figure 5 for 40 ms of data in the initial part of the second chorus wave packet in Figure 4, starting at 0849:30.620 UT. For this initial part we use a restricted frequency interval between 2.2 and 2.8 kHz to exclude higher-frequency components of the signal. The amplitude (Figure 5a) is plotted as average values in each subinterval of ≈1 ms (points) and also as the quadratic model functions on each subinterval (lines). Since the continuity of these model functions at boundaries between the neighboring subintervals is not build into the model, the fact that the obtained results are indeed continuous further demonstrates a good quality of fits. Each satellite first

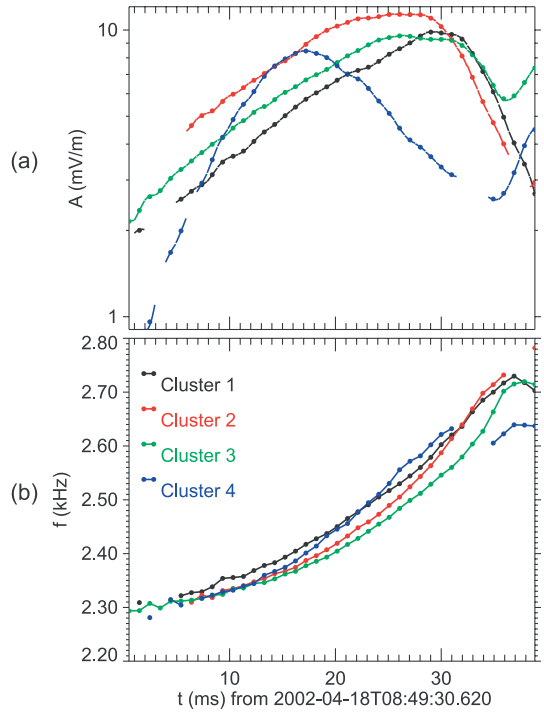


**Figure 5.** Model parameters in a 40-ms time interval in the beginning of the second chorus element in Figure 4. (a) Amplitude, (b) frequency. The results from the four spacecraft are color-coded.

observes an exponentially increasing amplitude, followed by a flat maximum and a decreasing amplitude. The maximum is observed significantly earlier by Cluster 4 (at $t = 17$ ms) than by the other spacecraft (around $t \approx 30$ ms). Also, the speed of the exponential increase is much higher at Cluster 4. The inverted *e*-folding time $\gamma$ of the exponential growth, $A = \mathcal{A}_0 \exp(\gamma t)$ ($calA_0$ being the amplitude at $t = 0$), is $\gamma \approx 180\ s^{-1}$ for Cluster 4 and $\gamma \approx 60\ s^{-1}$ for the other spacecraft. On the other hand, the subsequent decrease is slower on Cluster 4 ($\gamma \approx -80\ s^{-1}$) than on the others ($\gamma \approx -170\ s^{-1}$). With the theoretical group speed of $0.35c$ the *e*-folding distance for a hypothetical exponential convective growth or damping would be between 580 and 1750 km and the total distance traveled by the waves during the amplification phase would be 1200–2600 km. This would be roughly comparable to the estimates of the length of the interaction region. However, the evolution of the wave amplitude at the different spacecraft does not correspond to the sequence of spacecraft which would be encountered by a wave packet propagating antiparallel to $\boldsymbol{B}_0$.

[22] Evolution of the wave frequency is shown in Figure 5b. As we can expect from the spectrogram, the frequency grows for all the spacecraft in this time interval (except its final part which will be discussed later). The increase is again roughly exponential and it seems to be faster on Cluster 4. We can clearly see that the signal at the same frequency arrives at a different time on each of the different spacecraft. Taking now these arrival times as the basis for the examination of propagation of the wave packet and looking only at the growing phase of the wave amplitudes, we can see that the sequence of arrival times corresponds well to a wave packet propagating from the most northward Cluster 1 to the most southward Cluster 3 (Figure 3). This is consistent with the Poynting flux results in Table 1. The observed time delay between Cluster 1 and Cluster 3 is between 3 and 4 ms. This delay is higher than expected using the theoretical group speed, but it still is close to the predicted values taking into account the experimental errors. Note that when the amplitudes start to decrease (after $t \approx 20$ ms on Cluster 4 and after $t \approx 30$ ms on the other spacecraft), the sequence of arrival times is different and it no longer corresponds to a consistent propagation pattern from a convex-shaped source.

[23] A puzzling part of Figure 5 is a decrease of frequency and increase of amplitude in the end of the interval on some of the spacecraft. Figure 6 shows that the remainder of the time and frequency interval covering the entire chorus wave packet is even more puzzling. We use a 2.2–3.8 kHz pass band filter this time, and we can see that the results in the first 40-ms interval are very close to what we have presented in Figure 5 for a narrower analysis band. After this initial part where the different spacecraft observe a similar time-frequency structure, the results start to be very different. This is already seen on the waveforms of Cluster 2 (Figure 6a) which, in this case, observes the most intense waves reaching amplitudes of more than 30 mV/m, Cluster 3 (Figure 6b) which provides us with waveforms less polluted by higher-frequency signals, and Cluster 4 (Figure 6c) which showed different results already in the initial part of the chorus wave packet.

[24] The results of the amplitude (Figure 6d) and frequency (Figure 6e) estimations confirm that the same propagating chorus wave packet, appearing as nearly identical discrete chorus elements on the four spectrograms in Figure 4, has an internal fine structure which is different on the four spacecraft. The entire wave packet is composed of a number of subpackets appearing without any clear correlation in waveforms from the different spacecraft. In each of these subpackets the amplitude first increases (often exponentially), reaches a maximum, and finally decreases (often to very low values). For example, in Figure 6d, on Cluster 3 (green line) there is a subpacket from 0 ms to 36 ms, the second one 36–43 ms, then 43–48 ms, and 48–54 ms, then an intense one from 54 to 64 ms, then 64–67 ms, and so on. The frequency inside of each subpacket seems to behave independently and forms a rising trace, a falling trace, or a hook-shaped trace. In the majority of cases the frequency increases, most often in the final parts of the subpackets, making the whole chorus element, as it appears on the spectrograms, to grow in frequency from 2.3 kHz to 3.5 kHz during ≈90 ms.

[25] Figure 7 shows 6-s power spectrograms of chorus in the source region using the WBD data taken about 30 s later, when the spacecraft moved slightly northward and were located on both sides of the equator: Cluster 1 was to the north of it, and the other spacecraft were to the south. The upper band of chorus is reduced to a narrow-band emission just above $\frac{1}{2} f_{ce}$, seen in the first half of the interval. The chorus elements in the lower band appear more often than in the previous case. There is a significant correlation between the four spacecraft. Notably, the spectrograms of Cluster 1 and 2 are very similar. The spectrograms of Cluster 3 and 4 are more different but many common elements are still seen on the four spacecraft. It has been recently proven [*Santolík and Gurnett*, 2003] that the correlation is controlled by the

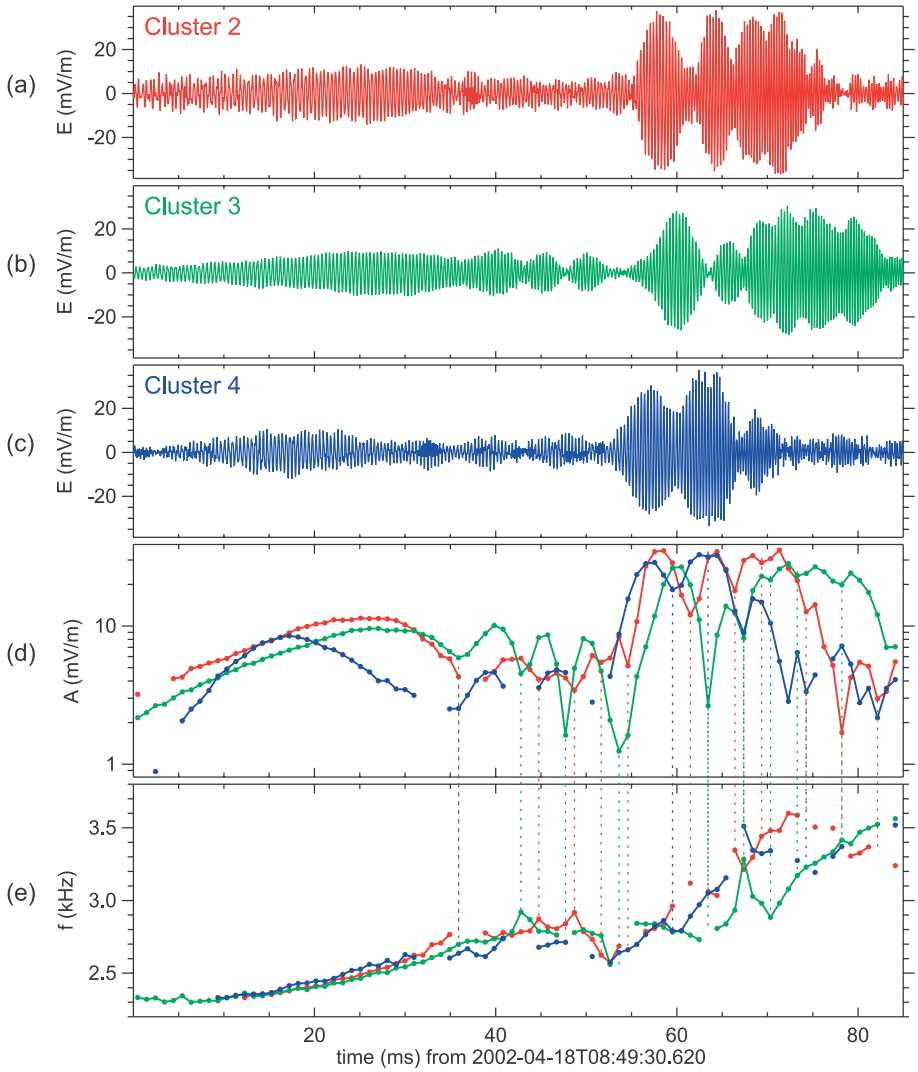


**Figure 6.** Waveforms and model parameters in an extended 85-ms time interval covering the second chorus element in Figure 4. (a–c) Broadband electric field waveform for Cluster 2–4, respectively; (d) Amplitude, (e) frequency. The results from the three spacecraft are color-coded. In order to demonstrate the fine structure, minima of amplitude are connected with the corresponding frequency estimates by vertical dotted lines.

separation of spacecraft measured in the plane perpendicular to $\boldsymbol{B}_0$. It has also been shown that in the 18 April 2002 case, the characteristic correlation length in this plane is of the order of 100 km. Indeed, Figure 3 shows that Cluster 3 and 4 are more separated in the perpendicular plane from the other spacecraft, while Cluster 1 and 2 are very close to each other (only about 6 km apart). Results of the propagation analysis using the STAFF-SA data are given in Table 2 for a 850-Hz frequency interval containing the lower band of chorus. Although not so significant as in Table 1, the Poynting flux consistently has a component oriented to the north (parallel to the $\boldsymbol{B}_0$ direction) on the four spacecraft, i.e., opposite to the previous case. The average wave vectors are again found approximately parallel to $\boldsymbol{B}_0$, with $\theta_{BK} \leq 10°$.

[26] Figure 8 presents results of our analysis of WBD waveforms for the chorus element denoted in Figure 7 by white arrows. It represents one of the cases where a chorus wave packet is simultaneously observed by Cluster 1 and 2 and not by the other two spacecraft. We use a 3–4 kHz passband filter and we again estimate the model parameters using a least squares fit. Similarly, as in the previous case, the amplitude observed by both satellites manifests a fine structure consisting of several subpackets. In spite of some common features this fine structure is different comparing the results from the two spacecraft. The amplitude often grows exponentially in the beginning of the subpackets with in a large range between 34 $s^{-1}$ and 420 $s^{-1}$. The overall frequency drift appears to be positive and approximately linear, and a wave of a given frequency is most often first detected by Cluster 2 and then by Cluster 1, with a typical delay of ≈2 ms. This value is close to the theoretical delay of 1.8 ms, and the propagation direction from Cluster 2 to Cluster 1 is consistent with the STAFF-SA results in Table 2.

[27] In Figure 9 we show the third 6-s example of power spectra, starting at 0852:28 UT. The four spacecraft moved further northward and were located at latitudes between 1°

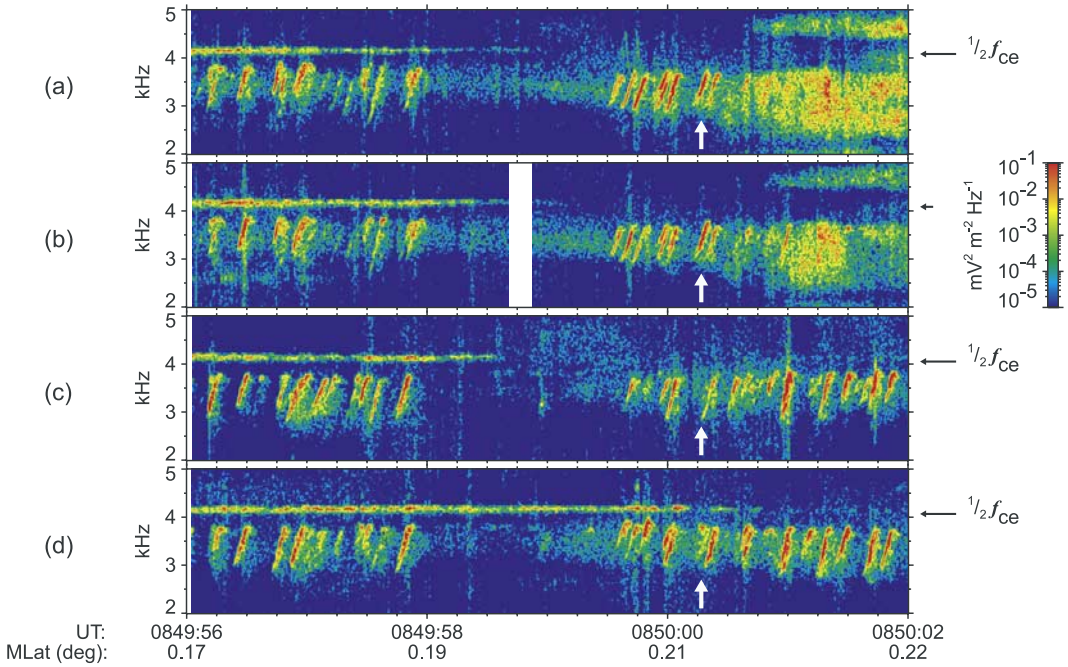


**Figure 7.** Detailed time-frequency power spectrograms of electric field fluctuations recorded by the WBD instruments on 18 April 2002 after 0849:56 UT. Figures 7a–7d show data from Cluster 1–4, respectively. Horizontal arrows on the right indicate local $\frac{1}{2} f_{ce}$ for each spacecraft. Position is given for Cluster 1 in the same way as in Figure 4 on the bottom. Bold white arrows point to the chorus element which is chosen for further analysis (see text).

and 1.6° north of the equator. The upper band of chorus, just above $\frac{1}{2} f_{ce}$, is now composed of many separate chorus elements with no clear correlation between the spacecraft. Only several elements in this band are similar on the first two spacecraft. The lower band, however, shows a very clear correlation of groups of chorus elements corresponding to wave packets simultaneously observed on the four spacecraft.

[28] The analysis of the STAFF-SA measurements in Table 3 shows quite indecisive results for the sign of the parallel component of the Poynting vector. The first three spacecraft give $S_{||}/\sigma S_{||}$ very close to zero, and Cluster 4 gives a positive value comparable to its standard deviation. The reason for this difference probably is that Cluster 4 accumulated the data during a slightly different interval of time. The wave vectors are again close to the field line on all the four spacecraft.

[29] In Figure 10 we demonstrate that the indecisive results of the analysis of the Poynting flux have a good explanation: Some chorus wave packets in that time interval propagate approximately southward (from Cluster 1 to Cluster 3) and the other wave packets propagate in the opposite direction. STAFF-SA instrument then accumulates the data during nearly 4 s and mixes the elements of both directions. The analysis therefore gives indecisive results concerning the sign of the parallel component of the Poynting flux. In Figure 10 we have analyzed two neighboring elements denoted by thick arrows below the spectrograms in Figure 9. Results from only two spacecraft, Cluster 1 and 3, are shown because of their largest parallel separation among the spacecraft pairs. We again find a fine structure of subpackets inside the two neighboring wave packets, which is reflected in the evolution of frequency in a similar way as

**Table 2.** Propagation Analysis for Chorus in Figure 7

| S/C | Time | Frequency | $S_{\|\|}/\sigma\ S_{\|\|}$ | $\theta_{BK}$ |
|---|---|---|---|---|
| 1 | 0849:58.60–0850:02.44 | 3175–4000 Hz | 1.4 | 4° |
| 2 | 0849:58.43–0850:02.27 | 3175–4000 Hz | 1.9 | 4° |
| 3 | 0849:58.21–0850:02.05 | 3175–4000 Hz | 1.7 | 10° |
| 4 | 0849:57.79–0850:01.63 | 3175–4000 Hz | 1.7 | 8° |

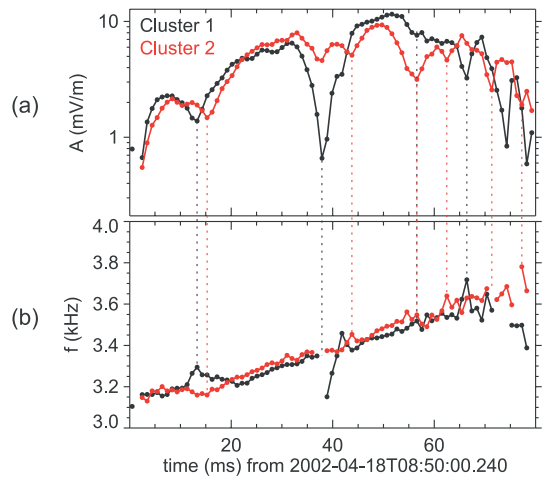


**Figure 8.** Model parameters in a 80-ms time interval covering the selected chorus element from Figure 7. (a) Amplitude, (b) frequency. The results from the Cluster 1 and Cluster 2 spacecraft are color-coded.

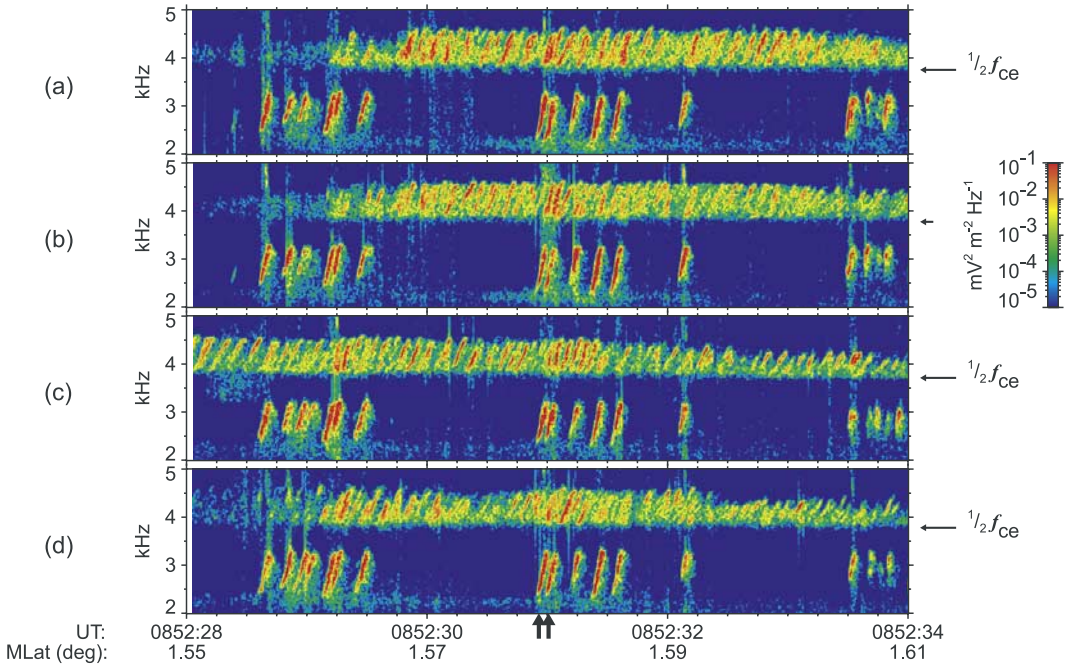


**Figure 9.** Power spectrograms of electric field fluctuations recorded by the WBD instruments on 18 April 2002 after 0852:28 UT. Figures 9a–9d show data from Cluster 1–4, respectively. Horizontal arrows on the right indicate local $\frac{1}{2} f_{ce}$ for each spacecraft. Position is given for Cluster 1 in the same way as in Figure 4 on the bottom. A pair of bold vertical arrows on the bottom point to the two chorus elements which are chosen for further analysis (see text).

in the previous examples. The long initial phase of the first wave packet consistently shows the waves at a given frequency coming first to Cluster 1 and then to Cluster 3. For the second wave packet after $t$ = 80 ms, the situation reverses. The time delays sometimes appear to be longer (up to ≈10 ms) than predicted by the theory (2.5 ms). A possible reason for this discrepancy could be the differences in internal structure of the wave packet observed by the two spacecraft.

## 4. Summary and Discussion

[30] We have analyzed nightside chorus emissions observed by the four Cluster spacecraft during a geomagnetically disturbed period on 18 April 2002. Chorus is observed in two bands separated by a gap near $\frac{1}{2} f_{ce}$, the upper band being only observed at latitudes within ≈5° from the geomagnetic equator.

[31] We have concentrated our analysis on the lower band, which extends to higher latitudes, decreasing in frequency. Poynting flux measurements in this band suggest that the chorus source region is located within ≈2000 km parallel to the field line. This distance is approximately equal to theoretical estimates of the length of the interaction region and to experimental estimates obtained for another similar case using analysis of frequency shifts (U. S. Inan, personal communication, 2002).

[32] The average wave vector directions in this region are nearly parallel to the field lines whereas at higher latitudes the wave vector directions gradually become inclined, as the waves propagate away from the source region.

[33] The dynamic character of the chorus source region is demonstrated by multipoint measurement of the Poynting flux where we observe nearly the same variation on the four

**Table 3.** Propagation Analysis for Chorus in Figure 9

| S/C | Time | Frequency | $S_\parallel/\sigma\ S_\parallel$ | $\theta_{BK}$ |
|---|---|---|---|---|
| 1 | 0852:30.59–0852:34.43 | 2520–3175 Hz | 0.04 | 12° |
| 2 | 0852:30.42–0852:34.26 | 2520–3175 Hz | 0.07 | 5° |
| 3 | 0852:30.21–0852:34.05 | 2520–3175 Hz | −0.07 | 6° |
| 4 | 0852:29.79–0852:33.63 | 2520–3175 Hz | 1.06 | 4° |

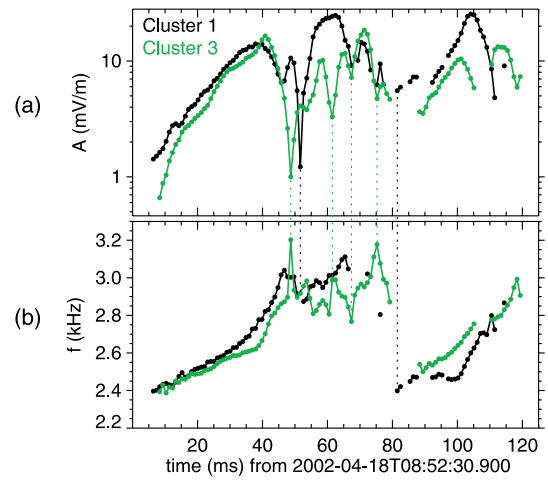


**Figure 10.** Model parameters in a 125-ms time interval covering the two selected chorus elements from Figure 9. (a) Amplitude, (b) frequency. The results from the Cluster 1 and Cluster 3 spacecraft are color-coded.

spacecraft at time scales of 4 s, although they are delayed by up to 1 min on their orbit.

[34] We have used a sine-wave parametric model with a variable amplitude to analyze the chorus waveforms with a time resolution better than 1 ms and with a frequency resolution better than 10 Hz. The principal assumption is the presence of a single wave frequency in each 1-ms subinterval of time and in a predefined frequency band. We have excluded all the data points where such a model does not fit the measured waveforms.

[35] The amplitude of the electric field waveforms reaches 30 mV/m, which would correspond to a 320-pT amplitude of the magnetic fluctuations, if we assume a whistler-mode refractive index of 3.2 estimated from the cold plasma theory. This rough estimate is ≈10 times higher than the saturation level of the magnetic field fluctuations observed in chorus elements by *Cornilleau-Wehrlin et al.* [1976] but only about 2 times larger then the maximum amplitudes observed by *Nunn et al.* [1997]. We are pursuing analysis of intervals when waveforms of magnetic field are measured and will report the results when they become available.

[36] The chorus wave packets, appearing as rising discrete elements on the power spectrograms, have an internal fine structure consisting of separate subpackets of variable lengths up to 40 ms. They seem to appear in the waveform in a random way without any clear periodicity.

[37] In the beginning of the majority of these subpackets we can detect an exponential growth phase which could be consistent with a linear instability [*Kennel and Petschek*, 1966; *Pasmanik et al.*, 2002] or with the linear growth of the triggered emissions [*Helliwell*, 1967]. However, the estimated large amplitudes of magnetic field fluctuations could imply strong nonlinear effects [*Nunn et al.*, 1997; *Trakhtengerts*, 1999] leading to an absolute instability with a faster growth which should appear, according to *Nunn et al.* [1997], already for amplitudes larger than a few pT. The observed growth coefficient $\gamma$ varies in a wide range of values, its ratio to the wave angular frequency $\gamma/\omega$ being of the order of a few thousandths to a few hundredths. After reaching the maximum amplitude, the subpackets often show an exponential decay phase with similar damping rates.

[38] Simultaneous observations on the four Cluster spacecraft show that even if chorus elements are well correlated on the power spectrograms at time scales of 0.1 s, their internal subpacket structure is different on the different spacecraft. This either means that the fine structure has a shorter characteristic dimension than a few tens of kilometers in the plane perpendicular to the ambient magnetic field (i.e., shorter than the typical perpendicular separation of the spacecraft) or else the fine structure changes along the field line at spatial scales of hundreds of kilometers. This second possibility means in other words that the fine structure changes during the propagation of the entire wave packet along the field line at temporal scales of a few ms. In any case the characteristic scales of the fine structure appears to be much lower than those of the chorus wave packet in which it is embedded. Because of these differences, it is often impossible to estimate the delay with which the wave packets arrive at the four spacecraft. However, in the initial growing phase of the chorus wave packet it is possible to find cases where the results are consistent with the sequence of spacecraft on the orbit. Their maximum separation parallel to the wave propagation direction, i.e., approximately along the field line, is a few hundreds of kilometers. To estimate the delays, we have used a criterion based on the wave frequency. The wave amplitudes do not seem to give consistent results even in the initial growing phase.

[39] Using these observed delays in the time-frequency plane, we have found the same propagation direction as obtained from the Poynting flux calculations based on simultaneous measurements of the electric and magnetic components. With some exceptions, caused probably by the differences in the fine structure, the delays roughly correspond to the whistler-mode group velocity estimated from the cold plasma theory. We have also observed delays corresponding to antiparallel propagation directions for two neighboring chorus elements separated by less than 0.1 s.

## Appendix A: Parametric Model of the Chorus Electric Field Signal

[40] In order to achieve a sufficient time and frequency resolution of analysis of chorus elements, we divide the electric field waveform, sampled at a frequency $f_s$, into short subintervals of $n$ samples. In each of these subintervals we use a nonlinear least-squares procedure to fit the parameters of a model of the electric field fluctuations. This model assumes the presence of a signal with a single frequency $f$ and a polynomially variable amplitude,

$$E(t, \boldsymbol{a}) = C + A(t)\,\sin[\,2\pi f(t - t_0) + \varphi\,], \tag{A1}$$

where $E$ is the model electric field at time $t$, $t_0$ is a reference time, $C$ is an offset value, $\varphi$ is the phase of the signal, and $A$ is the amplitude modeled by a quadratic polynom,

$$A(t) = A_0 + A_1\,(t - t_0) + A_2\,(t - t_0)^2. \tag{A2}$$

Six-dimensional vector

$$\boldsymbol{a} = (C, A_0, A_1, A_2, f, \varphi) \tag{A3}$$

then describes the model parameters. The reference time $t_0$ is defined as the middle of each subinterval, i.e., for the $i$th subinterval,

$$t_0 = \frac{1}{2}\left(\tau_{ni} + \tau_{[1+n(i-1)]}\right), \tag{A4}$$

where $\tau_k$ is time of the $k$th sample of the original waveform.

[41] The nonlinear least-squares procedure uses an iterative gradient expansion algorithm [*Press et al.*, 1992], and before each iteration we project the parameters of the model onto predefined convex intervals. The parameters $A_0$, $A_1$, and $A_2$, defining the quadratic approximation of the amplitude variations, are projected using the following relations:

$$-A_0 \rightarrow A_0, \varphi + \pi \rightarrow \varphi \quad \text{if} \quad A_0 < 0; \tag{A5}$$

$$A_0/\mathcal{T} \rightarrow A_1 \quad \text{if} \quad A_1 > A_0/\mathcal{T};$$
$$-A_0/\mathcal{T} \rightarrow A_1 \quad \text{if} \quad A_1 < -A_0/\mathcal{T}; \tag{A6}$$
$$-(A_0 - A_1\mathcal{T})/\mathcal{T}^2 \rightarrow A_2 \quad \text{if} \quad A_2 < -(A_0 - A_1\mathcal{T})/\mathcal{T}^2;$$
$$-(A_0 + A_1\mathcal{T})/\mathcal{T}^2 \rightarrow A_2 \quad \text{if} \quad A_2 < -(A_0 + A_1\mathcal{T})/\mathcal{T}^2, \tag{A7}$$

where $\mathcal{T}$ is one half of the duration of the subinterval

$$\mathcal{T} = \frac{1}{2}\left(\tau_{ni} - \tau_{[1+n(i-1)]}\right) = \frac{1}{2f_s}(n-1). \tag{A8}$$

The parameter $\varphi$ defining the phase of the signal is held in the interval $\langle 0, 2\pi)$ using

$$2\pi + \varphi \bmod 2\pi \rightarrow \varphi \quad \text{if} \quad \varphi < 0,$$
$$\varphi \bmod 2\pi \rightarrow \varphi \quad \text{if} \quad \varphi \geq 2\pi. \tag{A9}$$

The parameter $f$ defining the frequency of the signal is held in a predefined interval $\langle f_1, f_2\rangle$ using

$$f_2 \rightarrow f \quad \text{if} \quad f > f_2,$$
$$f_1 \rightarrow f \quad \text{if} \quad f < f_1. \tag{A10}$$

[42] To prevent convergence problems of the algorithm in cases where more than one frequency is present in the signal we, prior to the least-squares fit, pass the original waveform samples $\mathcal{E}_k$ through a nonrecursive digital pass-band filter selecting the frequency band between $f_1$ and $f_2$. The frequencies $f_1$ and $f_2$ are chosen on the case-by-case basis to contain the frequency range of the selected element and to exclude other emissions. The filtered waveform $\hat{E}_k$ is then divided into consecutive subintervals of $n$ data points. We estimate the relative difference of the filtered and original signals in the $i$th subinterval,

$$\mathcal{D} = \frac{100\%}{n \max_i\left(|\hat{E}|\right)} \sum_{j=1}^{n} |\, \mathcal{E}_{[n(i-1)+j]} - \hat{E}_{[n(i-1)+j]}\,|, \tag{A11}$$

where $\max_i(|\hat{E}|)$ is the maximum absolute value of the filtered data in the given subinterval.

[43] Each of the subintervals is separately used as input data in the least-squares procedure which iteratively improves estimates of model parameters $\boldsymbol{a}$ to obtain the minimum value of $\chi^2$. For the $i$th subinterval, $\chi^2$ reads

$$\chi^2 = \sum_{j=1}^{n} \left[\hat{E}_{[n(i-1)+j]} - E\left(\tau_{[n(i-1)+j]}, a\right)\right]^2 \sigma^{-2}_{[n(i-1)+j]}, \tag{A12}$$

where $\sigma_{[n(i-1)+j]}$ are errors on separate data points discussed below. The minimization procedure requires an initial estimate of the six model parameters which can be critical for the convergence. We thus run the iterative procedure 20 times, with randomly chosen initial $f$ and $\varphi$ parameters, $C$, $A_1$, and $A_2$ being initialized by zero, and $A_0$ by $\max_i(|\hat{E}|)$. If, in a given run, the decrease of $\chi^2$ from one successful iteration to the next one approaches numerical precision of the floating point representation, the convergence is reached, and the resulting minimum value $\chi^2_{\mathrm{m}}$ from equation (A12) is compared with the results of other runs. We then use the estimated parameters $\boldsymbol{a}_m$ for the lowest $\chi^2_{\mathrm{m}}$ obtained.

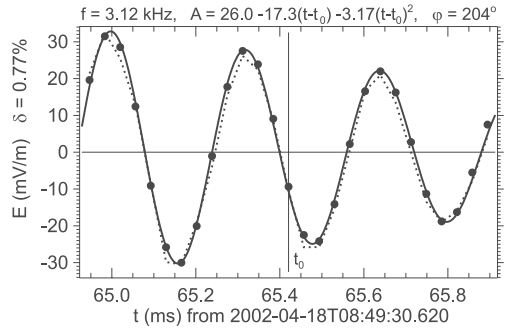


**Figure A1.** An example of fit of the model function to a short subinterval of Cluster 2 electric field data. (dotted line) Original broadband waveform; (filled circles) filtered waveform; (solid line) model function. Parameters resulting from the least-squares optimization are given on the top.

[44] Since the experimental errors $\sigma_{[n(i-1)+j]}$ on separate data points $\hat{E}_{[n(i-1)+j]}$ are difficult to estimate, we suppose

$$\sigma_{[n(i-1)+j]} = 1 \tag{A13}$$

for the minimization procedure. We are thus unable to use standard statistical $\chi^2$-distribution methods for quantifying how appropriate the model is for the given data. Instead we estimate how large should be the relative errors $\delta$ on the data if the model exactly fits the data points,

$$\delta = \frac{100\%}{\max_i\left(|\hat{E}|\right)} \sqrt{\frac{\chi^2_m}{n-6}}, \tag{A14}$$

where $n - 6$ is the theoretical mean value of the $\chi^2$-distribution.

[45] Figure A1 shows an example of results in a selected subinterval inside the second chorus element in Figure 4. We use the frequency interval between $f_1 = 2.2$ and $f_2 = 3.8$ kHz and we can see that the original waveform is very close to the filtered one. The signal from the chorus element thus dominates the broadband waveform with the maximum amplitude of more than 30 mV/m. The model fits very well to the data, with an average error less than 1%. The estimated frequency $f$, the quadratic model of the amplitude A (decreasing as a function of time), and the phase $\varphi$ are given on the top of the figure.

[46] The most important parameters for analyzing the chorus elements are frequency and amplitude. To obtain the same time resolution for the frequency and amplitude we calculate the average amplitude for each subinterval,

$$\bar{A} = \int_0^{\mathcal{T}} A(t)\, dt = A_0 + \frac{1}{3} A_2 \mathcal{T}^2, \tag{A15}$$

where $A(t)$ is from equation (A2), and we use $A_0$ and $A_2$ parameters from the final vector $\boldsymbol{a}_m$. A rough upper estimate

of the relative error on $\bar{A}$ is given by the relative error on the data points form equation (A14). This estimate is generally more conservative (gives higher values) than the calculation of errors on the model parameters from the covariance matrix using the second derivative of $\chi^2$ as a function of $\boldsymbol{a}_m$.

[47] Errors on estimated frequency are critical for determination of delays between the different spacecraft. We thus calculate a conservative estimate of the absolute error in frequency $\sigma_f$ using the data close to nulls of the model sine function in equation (A1). At those places we approximate $\sin(x)$ by $x$, and the relative error in frequency is

$$\delta_f = \frac{\sigma_f}{f} = \delta_T \approx \frac{\delta_E}{2\pi N}, \tag{A16}$$

where $\delta_T$ is the relative error in the estimated wave period, $N$ is the number of wave periods considered, and $\delta_E$ is the relative error in the data, approximated by the differences of the model and data normalized by the model amplitude. For the $i$th subinterval we obtain

$$\sigma_f = \frac{1}{2\pi n_{\mathcal{L}}} \frac{f}{N} \sum_{\ell \in \mathcal{L}} \frac{\left|\hat{E}_{[n(i-1)+\ell]} - E\left(\tau_{[n(i-1)+\ell]}, a_m\right)\right|}{A\left(\tau_{[n(i-1)+\ell]}\right)}, \tag{A17}$$

where $\mathcal{L}$ is a set of $n_{\mathcal{L}}$ indices for which the model signal is located near nulls of the model sine function in equation (A1). Those indices $\ell \in \mathcal{L}$ are selected from the interval $\langle 1, n \rangle$, where the absolute model values are below $\frac{1}{3}$ of the model amplitude,

$$\begin{gathered} \left|E\left(\tau_{[n(i-1)+\ell]}, \boldsymbol{a}_m\right)\right| < \frac{1}{3} A\left(\tau_{[n(i-1)+\ell]}\right), \\ A\left(\tau_{[n(i-1)+\ell]}\right) > \alpha \max_i (A). \end{gathered} \tag{A18}$$

Amplitude $A$ in equation (A17) is calculated using equation (A2) with the parameters $A_0$–$A_2$ from $\boldsymbol{a}_m$, $\max_i(A)$ is the maximum amplitude between the $n$ points in the $i$th subinterval, and we use $\alpha = 10^{-6}$ to take into account the finite numerical precision of calculations. Finally, ratio $f/N$ in equation (A17) can be estimated from the time interval between the first and the last null point of the model,

$$\frac{f}{N} = \left[\max_{\mathcal{L}} \left(\tau_{[n(i-1)+\ell]}\right) - \min_{\mathcal{L}} \left(\tau_{[n(i-1)+\ell]}\right)\right]^{-1}, \tag{A19}$$

where $\max_{\mathcal{L}}$ and $\min_{\mathcal{L}}$, respectively, give us the maximum and minimum time between the $n_{\mathcal{L}}$ indices in $\mathcal{L}$.

[48] Estimates of $\mathcal{D}$, $\delta$, and $\sigma_f$ can be used as measures of the reliability of results. We have thus set limits for their values within which we consider the resulting parameters of the model as reliable representation of properties of the original signal. If $\mathcal{D}$, $\delta$, or $\sigma_f$ does not fit within the predefined limits, we exclude the results obtained in a given subinterval from the summary plots and from further analysis. First, we do not allow the filtered signal to be by more than 50% different from the original waveform. This means that we exclude cases with stronger signal outside the predefined frequency interval than inside it. Second, we do not allow the model to be on average more deviated from the filtered waveform data than by 5%. In summary,

$$\begin{gathered} \mathcal{D} < 50\%, \\ \delta < 5\%, \end{gathered} \tag{A20}$$

where $\mathcal{D}$ and $\delta$ are obtained from equations (A11) and (A14), respectively. The second condition can be used to estimate the expected error on $f$; with the particular values of $n$ and $f_s$ we use throughout this study,

$$\begin{gathered} n = 27, \\ f_s = 27.44 \text{ kHz}, \end{gathered} \tag{A21}$$

we obtain the duration of $\approx$1 ms of each subinterval, and, at a typical frequency $f = 3$ kHz we have $N = 3$ wave periods per subinterval. When we then use $\delta$ in place of $\delta_E$ in equation (A16), we obtain the absolute accuracy better than 8 Hz on the frequency estimates. However, there can be cases when the model is more deviated from the data near its nulls than the average, and the frequency could have a larger random error. We therefore use a separate limit value for $\sigma_f$ from equation (A17) to make sure that the frequency estimates are accurate. The following third condition only applies to the estimates of the wave frequency $f$,

$$\sigma_f < 10 \text{ Hz}. \tag{A22}$$

[49] **Acknowledgments.** We thank J. Dowell, J. Seeberger, and R. Brechwald who prepared the preprocessing software for the WBD and R. Huff who made the WBD calibration. We thank P. Canu and P. Décréau (PI of Whisper) for useful information on the Whisper data. We acknowledge the access to the spin-resolution data of the FGM magnetic field experiment (PI A. Balogh) used for reference. The provisional Dst index and the quick-look AE index were obtained from WDC-C2, Kyoto University. We acknowledge discussions with V. Y. Trakhtengerts, R. Helliwell, and U.S. Inan. This work was supported by the NASA Goddard Space Flight Center under grant NAG5-9974. O. Santolík acknowledges additional support from grants GAUK 169/2002, MSM 113200004, and GACR 202/03/0832.

[50] Lou-Chuang Lee thanks David Nunn and Victor Trakhtengerts for their assistance in evaluating this paper.

## References

Anderson, R. R., and K. Maeda, VLF emissions associated with enhanced magnetospheric electrons, *J. Geophys. Res.*, *82*, 135–146, 1977.

Balogh, A., et al., The Cluster Magnetic Field Investigation: Overview of in-flight performance and initial results, *Ann. Geophys.*, *19*, 1207–1217, 2001.

Burtis, W. J., and R. A. Helliwell, Banded chorus—A new type of VLF radiation observed in the magnetosphere by OGO 1 and OGO 3, *J. Geophys. Res.*, *74*, 3002–3010, 1969.

Burton, R. K., and R. E. Holzer, The origin and propagation of chorus in the outer magnetosphere, *J. Geophys. Res.*, *79*, 1014–1023, 1974.

Canu, P., et al., Identification of natural plasma emissions observed close to the plasmapause by the Cluster-Whisper relaxation sounder, *Ann. Geophys.*, *19*, 1697–1709, 2001.

Cornilleau-Wehrlin, N., J. Etcheto, and R. K. Burton, Detailed analysis of magnetospheric ELF chorus: Preliminary results, *J. Atmos. Terr. Phys.*, *38*, 1201–1210, 1976.

Cornilleau-Wehrlin, N., et al., The Cluster spatio-temporal analysis of field fluctuations (STAFF) experiment, *Space Sci. Rev.*, *79*, 107–136, 1997.

Cornilleau-Wehrlin, N., et al., First results obtained by the Cluster STAFF experiment, *Ann. Geophys.*, *21*, 437–456, 2003.

Décréau, P. M. E., et al., Early results from the Whisper instrument on Cluster: An overview, *Ann. Geophys.*, *19*, 1241–1258, 2001.

Dunkel, N., and R. A. Helliwell, Whistler-mode emissions on the OGO 1 satellite, *J. Geophys. Res.*, *74*, 6371–6385, 1969.

Goldstein, B. E., and B. T. Tsurutani, Wave normal directions of chorus near the equatorial source region, *J. Geophys. Res.*, *89*, 2789–2810, 1984.

Gurnett, D. A., and B. J. O'Brien, High-latitude geophysical studies with Satellite Injun 3: 5. Very low frequency electromagnetic radiation, *J. Geophys. Res.*, *69*, 65, 1964.

Gurnett, D. A., et al., First results from the Cluster wideband plasma wave investigation, *Ann. Geophys.*, *19*, 1259–1272, 2001.

Gustafsson, G., et al., First results of electric field and density observations by Cluster EFW based on initial months of operation, *Ann. Geophys.*, *19*, 1219–1240, 2001.

Hattori, K., M. Hayakawa, D. Lagoutte, M. Parrot, and F. Lefeuvre, Further evidence of triggering chorus emissions from wavelets in the hiss band, *Planet. Space Sci.*, *39*, 1465–1472, 1991.

Hayakawa, M., Y. Yamanaka, M. Parrot, and F. Lefeuvre, The wave normals of magnetospheric chorus emissions observed on board GEOS 2, *J. Geophys. Res.*, *89*, 2811–2821, 1984.

Helliwell, R. A., *Whistlers and Related Ionospheric Phenomena*, Stanford Univ. Press, Palo Alto, Calif., 1965.

Helliwell, R. A., A theory of discrete emissions from the magnetosphere, *J. Geophys. Res.*, *72*, 4773–4790, 1967.

Kennel, C. F., and H. E. Petschek, Limit on stable trapped particle fluxes, *J. Geophys. Res.*, *71*, 1–28, 1966.

Lauben, D. S., U. S. Inan, T. F. Bell, D. L. Kirchner, G. B. Hospodarsky, and J. S. Pickett, VLF chorus emissions observed by Polar during the January 10, 1997 magnetic cloud, *Geophys. Res. Lett.*, *25*, 2995–2998, 1998.

LeDocq, M. J., D. A. Gurnett, and G. B. Hospodarsky, Chorus source locations from VLF Poynting flux measurements with the Polar spacecraft, *Geophys. Res. Lett.*, *25*, 4063–4066, 1998.

Meredith, N. P., R. B. Horne, A. D. Johnstone, and R. R. Anderson, The temporal evolution of electron distributions and associated wave activity following substorm injections in the inner magnetosphere, *J. Geophys. Res.*, *105*, 12,907–12,917, 2000.

Nagano, I., S. Yagitani, H. Kojima, and H. Matsumoto, Analysis of wave normal and Poynting vectors of the chorus emissions observed by Geotail, *J. Geomagn. Geoelectr.*, *48*, 299–307, 1996.

Nunn, D., Y. Omura, H. Matsumoto, I. Nagano, and S. Yagitani, The numerical simulation of VLF chorus and discrete emissions observed on the Geotail satellite using a Vlasov code, *J. Geophys. Res.*, *102*, 27,083–27,097, 1997.

Omura, Y., D. Nunn, H. Matsumoto, and M. J. Rycroft, A review of observational, theoretical and numerical studies of VLF triggered emissions, *J. Atmos. Terr. Phys.*, *53*, 351–368, 1991.

Parrot, M., O. Santolík, N. Cornilleau-Wehrlin, M. Maksimovic, and C. Harvey, Source location of chorus emissions observed by CLUSTER, *Ann. Geophys.*, *21*, 473–480, 2003.

Pasmanik, D. L., A. G. Demekhov, D. Nunn, V. Y. Trakhtengerts, and M. Rycroft, Cyclotron amplification of whistler-mode waves: A parametric study relevant to discrete VLF emissions in the Earth's magnetosphere, *J. Geophys. Res.*, *107*(A8), 1162, doi:10.1029/2001JA000256, 2002.

Press, W. H., B. P. Flannery, S. A. Teukolsky, and W. T. Vetterling, Numerical Recipes, Cambridge Univ. Press, New York, 1992.

Samson, J. C., Descriptions of the polarization states of vector processes: Applications to ULF magnetic fileds, *Geophys. J. R. Astron. Soc.*, *34*, 403–419, 1973.

Santolík, O., and D. A. Gurnett, Transverse dimensions of chorus in the source region, *Geophys. Res. Lett.*, *30*(2), 1031, 10.1029/2002GL016178, 2003.

Santolík, O., F. Lefeuvre, M. Parrot, and J. L. Rauch, Complete wave-vector directions of electromagnetic emissions: Application to INTERBALL-2 measurements in the nightside auroral zone, *J. Geophys. Res.*, *106*, 13,191–13,201, 2001.

Santolík, O., M. Parrot, and F. Lefeuvre, Singular value decomposition methods for wave propagation analysis, *Radio. Sci.*, *38*(1), 1010, 10.1029/2000RS002523, 2003.

Sazhin, S. S., and M. Hayakawa, Magnetospheric chorus emissions: A review, *Planet. Space Sci.*, *40*, 681–697, 1992.

Skoug, R. M., S. Datta, M. P. McCarthy, and G. K. Parks, A cyclotron resonance model of VLF chorus emissions detected during electron microburst precipitation, *J. Geophys. Res.*, *101*, 21,481–21,491, 1996.

Smith, A. J., and D. Nunn, Numerical simulation of VLF risers, fallers, and hooks observed in Antarctica, *J. Geophys. Res.*, *103*, 6771–6784, 1998.

Stix, T. H., *Waves in Plasmas*, Am. Inst. of Phys., New York, 1992.

Storey, L. R. O., An investigation of whistling atmospherics, *Phil. Trans. Roy. Soc. London*, *A246*, 113–141, 1953.

Trakhtengerts, V. Y., A generation mechanism for chorus emission, *Ann. Geophys.*, *17*, 95–100, 1999.

N. Cornilleau-Wehrlin, CETP, 10/12 Avenue de L'Europe, F-78140 Vélizy, France. (nicole.cornilleau@cetp.ipsl.fr)

D. A. Gurnett and J. S. Pickett, Department of Physics and Astronomy, University of Iowa, Iowa City, IA 52242-1479, USA. (gurnett@space.physics.uiowa.edu; jsp@space.physics.uiowa.edu)

M. Parrot, LPCE/CNRS, 3A Avenue de la Recherche, Orléans, F-45071 France. (mparrot@cnrs-orleans.fr)

O. Santolík, Faculty of Mathematics and Physics, Charles University, V Holešovičkách 2, CZ-18000 Praha 8, Czech Republic. (ondrej.santolik@mff.cuni.cz)